JGR Oceans

RESEARCH ARTICLE
10.1029/2024JC021132

Special Collection:
The Arctic Ocean's changing Beaufort Gyre

Pacific-Arctic Connections: Assessing Flow Through Bering Strait in Context With Dynamic Ocean Topography and Surface Stress

Annika Margevich[1], **Mary-Louise Timmermans**[1], **and Seth Danielson**[2]

[1]Department of Earth and Planetary Sciences, Yale University, New Haven, CT, USA, [2]College of Fisheries and Ocean Sciences, University of Alaska Fairbanks, Fairbanks, AK, USA

Abstract Bering Strait is the only ocean gateway connecting the Pacific and Arctic oceans. The ~1 Sv northward flow of Pacific water through the strait to the Arctic Ocean has been increasing by ~0.01 Sv/yr since 1990. Monthly dynamic ocean topography (DOT), wind, and sea-ice data at Bering Strait are analyzed in context with the long-term record of flow through the strait to investigate local drivers. Ocean transport is found to be proportional to the across-strait slope in DOT, suggesting some component of the flow is in geostrophic balance. Along-strait ocean surface stresses, which modulate the across-strait DOT slope via Ekman transport, are analyzed in the presence of a seasonally varying ice cover. It is shown that northward interior ocean flow under sea ice in winter results in southward surface stresses, and westward Ekman transport that slows the geostrophic component of the northward ocean flow. As the number of open water days local to Bering Strait increase each year, we find no trend in the annual mean surface stress, that is, the loss of sea ice is not leading to increased northward wind stress input that would enhance northward ocean flow. This analysis is consistent with the theory that changes in both the atmosphere and ocean non-local to Bering Strait are likely driving the increased transport from the Pacific into the Arctic via Bering Strait.

Plain Language Summary Bering Strait is a narrow waterway, 50 m deep and 85 km wide, between Alaska and Russia that allows relatively warmer and fresher Pacific water to flow into the Arctic Ocean. The volume of water entering the Arctic through Bering Strait has increased approximately 30% since 1990. It is unclear what processes are responsible for this observed increase. We determine that part of Bering Strait throughflow is driven by the difference in pressure across the strait, or an across-strait slope in sea surface, which can be caused by a stress applied parallel to the strait. When winds blow to the north, water piles up on the Alaskan side creating a pressure difference that is proportional to the flow. When sea ice is absent, winds act directly on the ocean. When sea ice is present, sea ice applies a stress onto the ocean. We find that as the Arctic loses sea ice, there are no changes in stress due to fewer days of sea ice cover. This suggests that local winds and sea ice are not driving the increase in transport, and that large-scale changes in the Pacific and Arctic Oceans are driving the increase in transport through Bering Strait.

Key Points:

- Monthly dynamic ocean topography (DOT) supports that some component of flow through Bering Strait is in geostrophic balance
- Local surface stress in Bering Strait increases to the south as the interior flow increases to the north when sea ice is present
- The increasing number of open water days each year is not contributing to enhanced northward transport via increased wind stress input

Supporting Information:

Supporting Information may be found in the online version of this article.

Correspondence to:

A. Margevich,
annika.margevich@yale.edu

Citation:

Margevich, A., Timmermans, M.-L., & Danielson, S. (2024). Pacific-Arctic connections: Assessing flow through Bering Strait in context with dynamic ocean topography and surface stress. *Journal of Geophysical Research: Oceans*, *129*, e2024JC021132. https://doi.org/10.1029/2024JC021132

Received 19 MAR 2024
Accepted 5 AUG 2024

Author Contributions:

Conceptualization: Annika Margevich, Mary-Louise Timmermans
Data curation: Annika Margevich
Formal analysis: Annika Margevich, Mary-Louise Timmermans
Funding acquisition: Mary-Louise Timmermans
Investigation: Annika Margevich, Mary-Louise Timmermans, Seth Danielson
Methodology: Annika Margevich, Mary-Louise Timmermans, Seth Danielson
Project administration: Mary-Louise Timmermans
Resources: Mary-Louise Timmermans, Seth Danielson

1. Introduction

Bering Strait lies between Alaska and Russia and connects the Northeastern Pacific Ocean to the Arctic Ocean. It is the only source of Pacific inflow to the Arctic Ocean and, therefore, is particularly influential to the downstream Chukchi Shelf and Canada Basin. The strait is ~50 m deep and ~85 km wide, supporting a northward throughflow of approximately 1 Sv = 10^6 m^3/s (Roach et al., 1995; Woodgate, 2018). The Pacific inflow serves as a source of relatively fresh water to the western Arctic Ocean, accounting for approximately one-third of the freshwater input to the Arctic (Aagaard & Carmack, 1989; Serreze et al., 2006). Bering Strait inflow also carries approximately 3–6 × 10^{20} J/yr (relative to freezing temperature) of heat in the spring and summer from the Pacific to the Arctic (Shaw et al., 2009; Shimada et al., 2006; Woodgate et al., 2010). This incoming warm and fresh water influences the larger Arctic system. For example, the freshwater influences the regional stratification, and the incoming heat has been shown to be important in initiating the sea-ice albedo feedback (Lu et al., 2020; Serreze et al., 2016; Woodgate et al., 2010). Over the last three decades, volume transport through Bering Strait has been increasing at ~0.01 Sv/yr (Woodgate, 2018). Here we explore drivers of the Bering Strait inflow such that we might better understand how future climate change will influence the Pacific-Arctic system.

Supervision: Mary-Louise Timmermans, Seth Danielson
Validation: Annika Margevich
Visualization: Annika Margevich
Writing – original draft: Annika Margevich, Mary-Louise Timmermans, Seth Danielson
Writing – review & editing: Annika Margevich, Mary-Louise Timmermans, Seth Danielson

The forcing behind the Bering Strait throughflow is often split into two components: a pressure head component and a local-wind component. The pressure head component relates to higher sea surface heights (SSH) in the Pacific than in the Arctic (Aagaard et al., 1981; Coachman & Aagaard, 1966). Aagaard et al. (2006) argue that the pressure head is of steric origin. More recent studies have used a variety of in situ, model, remotely sensed, and reanalysis data to explore how the Pacific-Arctic pressure head operates on different temporal and spatial scales and how the large-scale forcing relates to flow through Bering Strait. Danielson et al. (2014) propose that Arctic and sub-Arctic atmospheric pressure fields (e.g., the Siberian High and Aleutian Low) both contribute to Bering Strait flow variations through a combination of direct wind forcing and altered SSH gradients that arise from cross-shore Ekman transport in both the Bering Sea and the East Siberian Sea (ESS). Along-shore winds drive coastal Ekman convergences and divergences that contribute to regional SSH gradients and associated along-shore and through-strait flows (Danielson et al., 2014). Peralta-Ferriz and Woodgate (2017) examine the ESS in greater detail, identifying a temporally shifting control of the Bering Strait flow that seasonally relocates between the ESS and the Bering Sea. Nguyen et al. (2020) use an adjoint model to explore how local and remote atmospheric forcings relate to flow through Bering Strait. They further affirm that on monthly time scales, both the ESS and the Bering Sea are influential in setting variability in flow through Bering Strait. Similarly, Zhang et al. (2020) use a model to show that winds over the ESS and the Bering Sea influence the SSH gradient between the two basins which ultimately influences the flow through Bering Strait. Another proposed theory for the pressure head posits that it is set up between the North Pacific and the North Atlantic where the lack of deep water formation in the Pacific allows higher sea surface elevations there than in the Atlantic (Cessi, 2020). The consensus, though, seems to be that the Bering Sea and the ESS are important centers of action with respect to the large-scale forcings behind the Pacific-Arctic pressure head that partially drives the Bering Strait throughflow.

The second component forcing Bering Strait throughflow is associated with the local winds. This component has been identified through the correlation between local winds and transport through Bering Strait. In the winter when volume transport is weaker, that is, ∼0.4 Sv, there is a strong correlation between northward transport and the strong southward winds (Woodgate, 2018). This suggests that Ekman transport may play a role, where strong winds from the north reduce northward transport by increasing westward Ekman transport across the strait (Woodgate, 2018). In the summer, when flow through the strait is ∼1.3 Sv, there is only a moderate correlation between northward transport and the weak northward surface winds. This seasonality in the correlation between transport and the local winds has led to the assumption that the pressure head is the primary mechanism driving flow through the strait in summer and local wind forcing is the dominant driver for the flow in winter (Woodgate, 2018). While it is likely that local winds influence Bering Strait throughflow in the winter, the presence of sea ice has not yet been considered when exploring these local surface dynamics.

Bering Strait is sea-ice covered from around late November until June, where the influence of this seasonal ice cover on the local surface dynamics contributing to flow through Bering Strait is largely unknown. The complicated effect of sea-ice cover in the presence of a sustained ocean flow has been explored, for example, in the context of the anticyclonic wind-driven Beaufort Gyre (e.g., Meneghello et al., 2018). When the ice pack is less concentrated and more mobile (summer), anticyclonic wind forcing drives convergent Ekman transport, spinning up the gyre. Conversely, in the presence of a concentrated, relatively immobile ice pack (winter), friction between the anticyclonic geostrophic ocean flow and the slower sea ice drives a divergent Ekman transport, relaxing the gyre (Dewey et al., 2018; Meneghello et al., 2018; Proshutinsky et al., 2002). Analogous seasonal dynamics may have some influence on northward flow through Bering Strait.

In this study, we focus on the Bering Strait region and analyze dynamic ocean topography (DOT) in addition to mooring data, wind reanalysis and sea ice data to assess the Bering Strait flow dynamics. We explore how the seasonal presence of sea ice influences the surface stress in Bering Strait and how the loss of sea ice might be affecting ocean transport. In Section 2, the data are described, and the methods for characterizing the across- and along-strait DOT slopes and the surface stresses are explained. Section 3 outlines the equations of motion in the across- and along-strait directions and assesses the across-strait balance using observations. Section 4 discusses how the presence of sea ice relates to the correlation between local winds and northward transport and assesses whether the loss of sea ice in Bering Strait relates to the observed increase in northward transport. Finally, Section 5 summarizes and discusses these results.

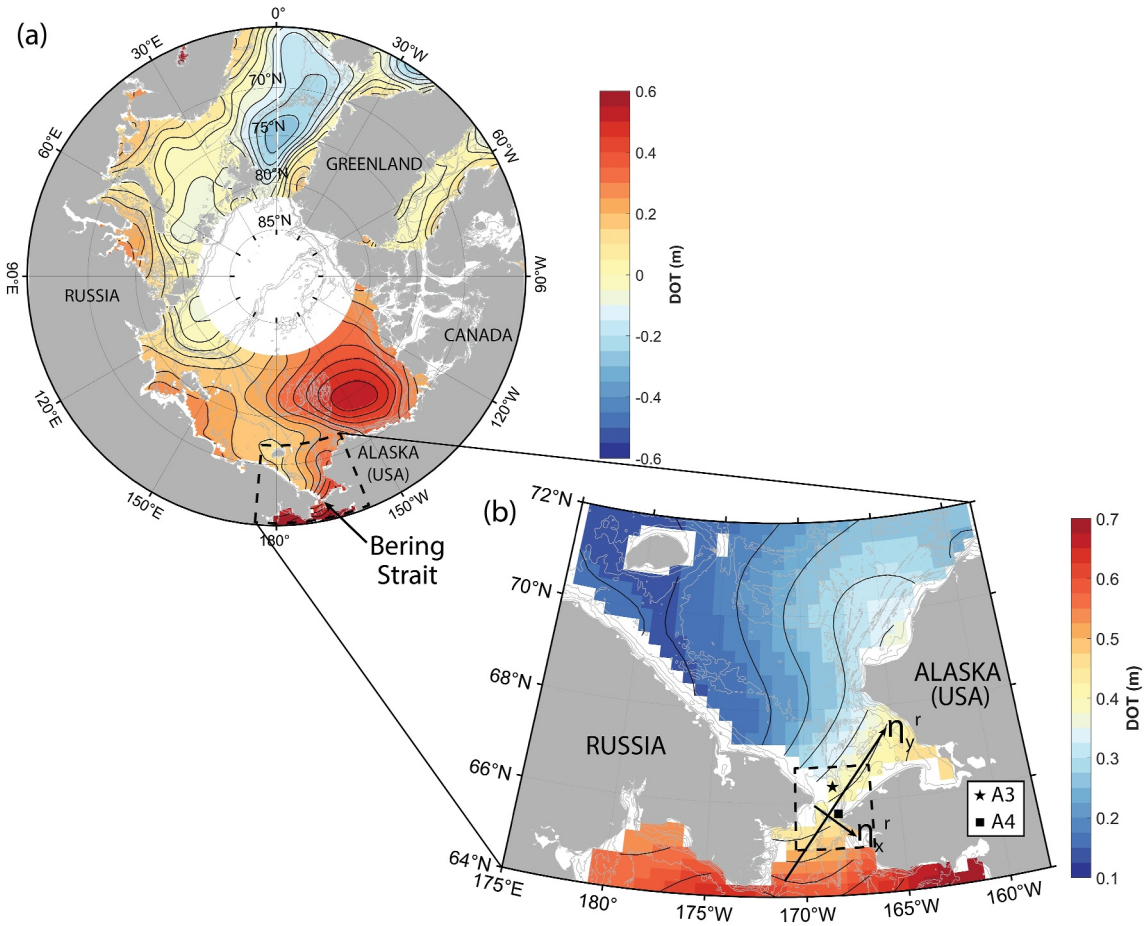

Figure 1. (a) Mean dynamic ocean topography (DOT) field across the Arctic over 2003–2014. The dashed line outlines the region shown in Figure 1b. (b) Mean DOT field in the Bering Strait Region over 2003–2014. The dashed line outlines the region over which wind, sea ice concentration, and surface stress are averaged. Arrows indicate the directions of the across-strait, $\eta_x{}^r$, and along-strait, $\eta_y{}^r$, slopes. The locations of the A3 and A4 moorings are indicated by the black star and square, respectively. Black lines are DOT contours and gray lines are bathymetry.

2. Data and Methods

2.1. Dynamic Ocean Topography

The monthly DOT data are from the Centre for Polar Observation and Modeling (CPOM), which uses satellite altimetry data from the Envisat and CryoSat-2 missions (Armitage et al., 2016, 2017) (Figure 1). Satellite altimetry measures the distance from the satellite to the surface of the ocean. DOT is calculated by subtracting the altimetry reading from the distance between the satellite and an assumed reference geoid (the GOCO03s geoid in this case). In the presence of sea ice, DOT can be estimated by using leads and other open-water areas to determine the distance between the satellite and the ocean surface rather than the ice surface. The CPOM DOT data span 2003–2014 at monthly time intervals. The spatial coverage is 60°N–81.5°N on a 0.75° × 0.25° grid. The "pole hole" is defined as north of 81.5°N to ensure compatibility between the two satellite missions. Average uncertainties associated with the sea-surface height measurements used to calculate DOT are ∼1.1 cm for the monthly means and ∼0.9 cm for the annual means (Armitage et al., 2016).

In recent years, two additional DOT data sets have been released, both using the CryoSat-2 satellite mission and covering up to 88°N monthly from 2011 through 2020 (Doglioni et al., 2023; Lin et al., 2023). Differences between these data include differing geoid models and grids. Doglioni et al. (2023) use the Optimal Geoid for Modeling Ocean Circulation (OGMOC) geoid model and is on a 0.75° × 0.25° grid while Lin et al. (2023) use the GOCO03s geoid model and a polar stereographic projection. Each of these data sets has a different grid through

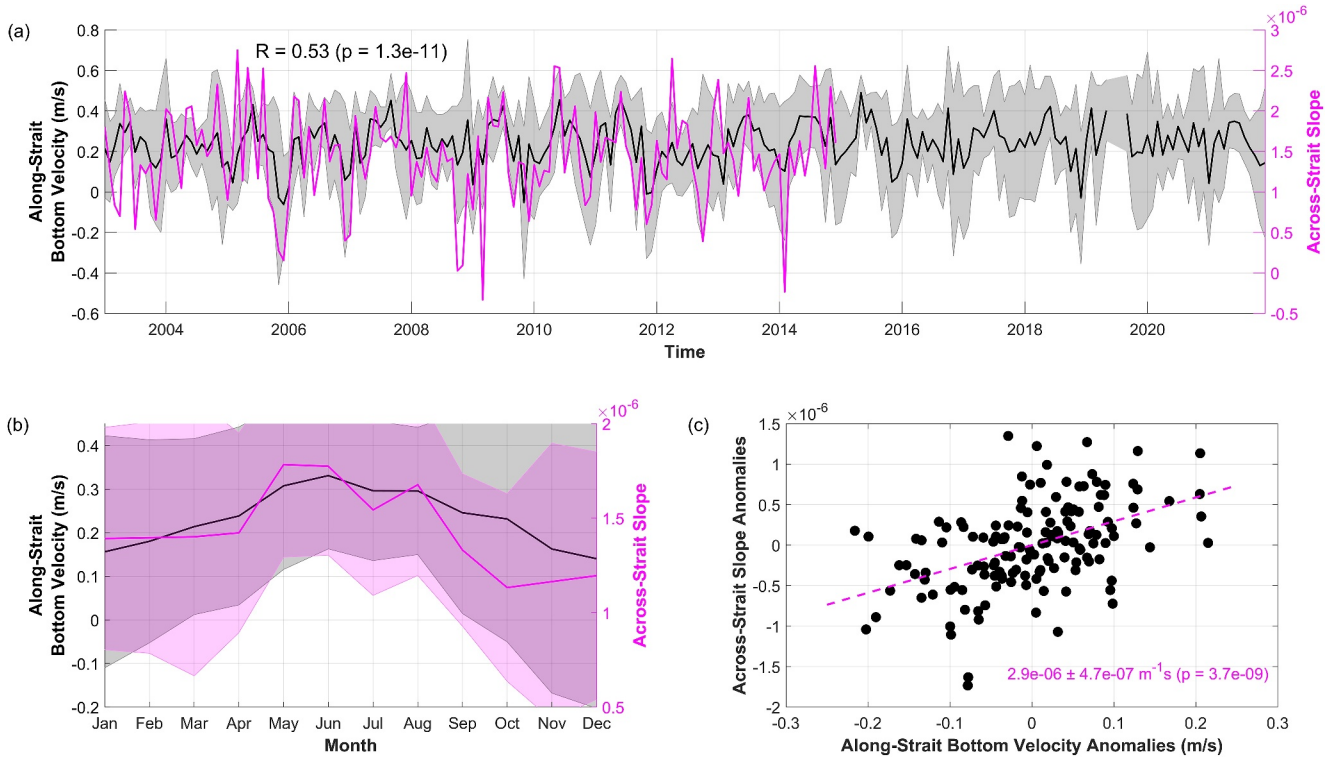

Figure 2. (a) Monthly mean time series of the along-strait bottom velocity (black) from 2003–2021 and the monthly across-strait slope from dynamic ocean topography (magenta) from 2003–2014. The correlation coefficient between the along-strait bottom velocity and the across-strait slope is shown as $R = 0.53$ ($p = 1.34\text{e}{-11}$). (b) Monthly climatology for along-strait bottom velocity through Bering Strait from the A3 mooring for 2003–2014 (black) and for the across-strait slope over 2003–2014 (magenta). Shading is one standard deviation. (c) Anomalies from the monthly climatology in along-strait bottom velocity versus across-strait slope from 2003–2014. The magenta dashed line shows the linear regression with 99% confidence.

Bering Strait compared to that of Armitage et al. (2016), neither of which have grid boxes oriented across Bering Strait that could be used to compute the across-strait slope in more recent years.

The across-strait slope, $\eta_x{}^r$, is the change in DOT between the Russian coast and the Alaskan coast at the narrowest point of Bering Strait. To compute this across-strait slope, we rotate the frame of reference such that $\eta_x{}^r$ is approximately perpendicular to the DOT contours through Bering Strait (Figure 1b), which is a 45° clockwise rotation. Variables with a superscript of r indicate the value is calculated in this rotated frame. It follows that the along-strait slope, $\eta_y{}^r$, is perpendicular to $\eta_x{}^r$. We rotate the wind, ice, and water velocities to be in the same frame of reference. From the DOT field, we calculate a monthly time series of $\eta_x{}^r$ using a linear regression over the three grid boxes in the across-strait direction at every monthly interval (Figure 2a) from which we can determine the seasonality of the across-strait slope (Figure 2b) and the monthly anomalies (Figure 2c). To compute $\eta_y{}^r$, we define a transect perpendicular to the across-strait slope. We identify the latitude along the transect at which the DOT change is steepest and take this to be the center of the along-strait DOT slope. We then compute $\eta_y{}^r$ from a linear regression over the points within ~1° latitude north and south of the center of the slope over the along-strait transect.

2.2. Mooring Data

Ocean velocity data through Bering Strait are from year-round bottom tethered ocean moorings, specifically the A3 mooring located just north of Bering Strait (Figure 1b), which is one of several long-term moorings in the Bering Strait region (Woodgate, 2018; Woodgate et al., 2015; Woodgate & Peralta-Ferriz, 2021). Because the Diomede Islands split Bering Strait into a western and eastern channel, data from the A3 mooring is taken to approximate water properties and transport through Bering Strait as a whole. For this reason, it is referred to as the "climate site" (Woodgate, 2018). From 1990 through 2006, velocities in the lower layer at ~45 m depth were measured by an Aanderaa single point current meter (RCM) every hour, where the water depth at A3 is ~57 m

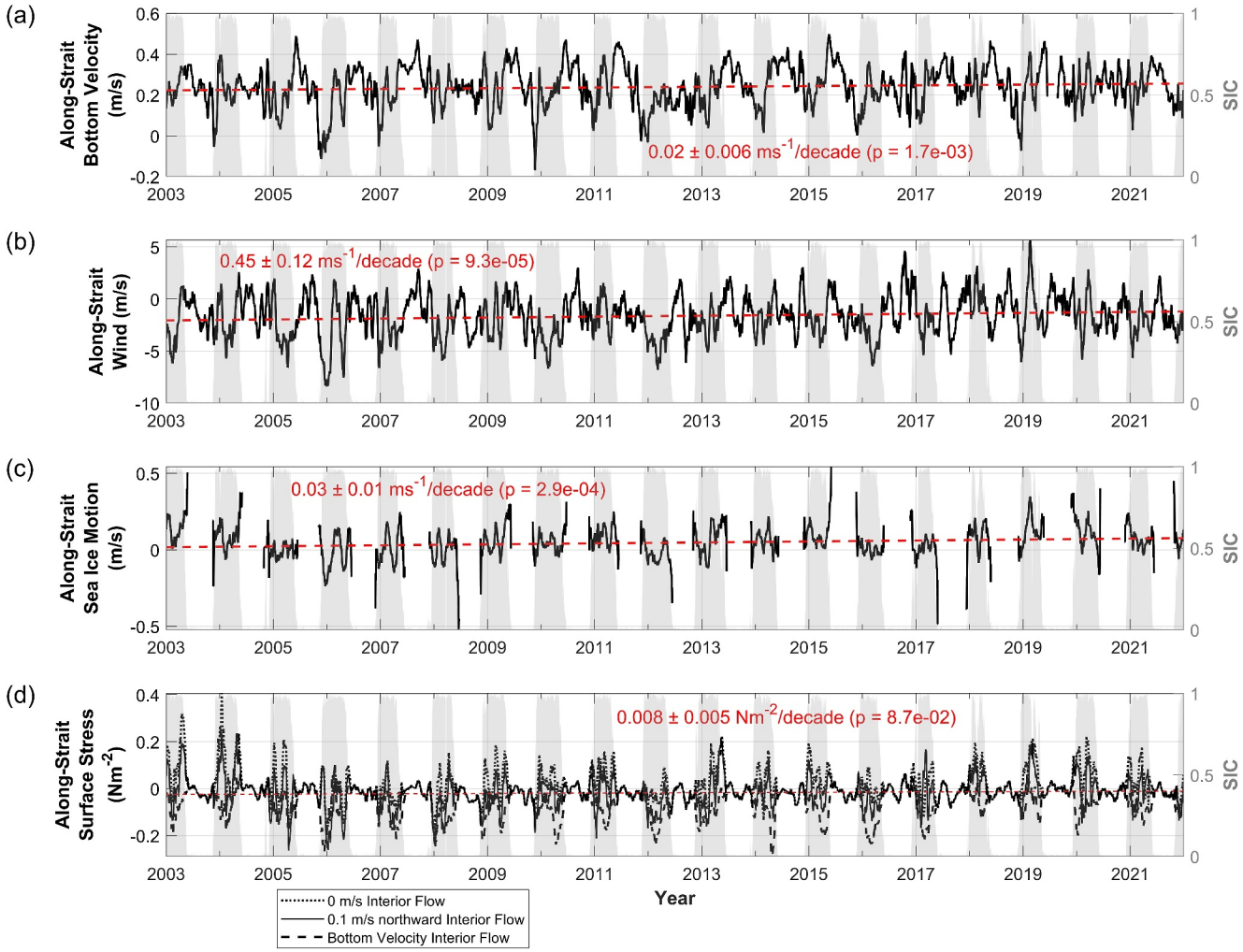

Figure 3. 30-day running average over 2003–2021 of the (a) along-strait bottom velocity, (b) along-strait winds, (c) along-strait sea ice motion, and (d) along-strait surface stress assuming no interior flow (dotted), an interior flow of 0.1 m/s to the north (solid), and an interior flow equal to that of the bottom velocity (dashed). Positive (negative) values in each case indicate northward (southward) direction. The gray shading is daily sea ice concentration local to Bering Strait over the same time frame. Red dashed lines indicate statistically significant trends with the associated p-value indicated on each panel. In panel (d), the trend shown corresponds to surface stress calculated assuming the interior flow is 0.1 m/s to the north. There is no statistically significant trend assuming zero interior flow, and surface stress calculated assuming an interior flow equal to the bottom velocity shows a trend with a slope of 0.006 ± 0.003 N/m^2/decade (p = 5.8e−02).

(Woodgate, 2018). Beginning in 2007, velocities throughout the water column are measured by an acoustic Doppler current profiler (ADCP) every 30 min. To maintain continuity between the RCM and ADCP data, we use velocity data from the second lowest-depth bin of the ADCP data as bottom velocity and interpolate it onto an hourly grid. As a note, the lowest-depth bin of the ADCP data is neglected due to recording erroneously low velocity values (Woodgate, 2018). We de-tide the hourly velocities using the t_{tide} function in Matlab (Pawlowicz et al., 2002) and take daily averages of the detided hourly data. Because we use a rotated frame of reference for the across- and along-strait slopes, we rotate the bottom velocities clockwise by 45° for consistency (Figure 3a); terms along-strait and across-strait refer to the coordinate axes drawn in Figure 1b. Using the rotated bottom velocity and assuming flow is barotropic and horizontally homogeneous, we estimate volume transport from the A3 mooring by multiplying the rotated velocity by a cross-section area of 4.25 km^2 (Woodgate, 2018).

Sea ice motion data are from under-ice-tracking ADCPs mounted on the year-round bottom tethered ocean moorings at sites A3 and A4 (Figure 1b). The A4 mooring has under-ice-tracking ADCP data from mid-2002 to the present, while the A3 mooring has ADCP data spanning mid-2007 to the present. Because the A3 site is considered the climate site, we use the under-ice-tracking ADCP data from A3 for 2007–2021. We then fill any gaps in the A3 time series over 2003–2021 with data from the under-ice-tracking ADCP on the A4 mooring, as there is relatively

good agreement in sea ice motion between the two moorings (Figure S1 in Supporting Information S1). Similar to the bottom velocity data, we de-tide hourly sea ice velocities using the t_{tide} function in Matlab (Pawlowicz et al., 2002) and take daily averages of the detided hourly data. We apply a threshold of 0.7 m/s for sea ice speeds, as values exceeding this threshold tend to be associated with short-lived spurious fluctuations. Additionally, we only consider under-ice-tracking ADCP data at times when the sea ice concentration is greater than 0.15 (Cavalieri et al., 1991). Smoothed daily time series for the resulting sea ice motion data are shown in Figure 3c.

2.3. Wind and Sea-Ice Concentration Data

The 10 m wind field data are from the ERA5 Reanalysis hourly fields with a resolution of 0.25° × 0.25° (Hersbach et al., 2023). Daily sea ice concentration data are obtained from the National Oceanic and Atmospheric Administration (NOAA) and National Snow and Ice Data Center (NSIDC) Climate Data Record of Passive Microwave Sea Ice Concentration, Version 4 (Meier et al., 2021). We regrid the sea ice concentration data onto the same 0.25° × 0.25° grid as the 10 m ERA5 winds. We then compute the mean 10 m winds and sea ice concentration over 65°N–66.75°N and 189.5°E–193.5°E (dashed box in Figure 1b). Smoothed daily time series for these variables are shown in Figure 3b.

2.4. Quantifying Surface-Ocean Stresses

Bering Strait is ice-covered between approximately November and June each year. To account for the effect of seasonal sea ice cover in Bering Strait on the local surface stress, we characterize surface stress as

$$\boldsymbol{\tau}_{\mathbf{sfc}} = SIC\rho C_{ice}|\mathbf{u_{rel}}|(\mathbf{u_{rel}}) + (1 - SIC)\rho_a C_{air}|\mathbf{u_{air}}|(\mathbf{u_{air}}), \quad (1)$$

where SIC is the ice concentration local to Bering Strait; ρ is the density of water, taken as $\rho = 1{,}027.5$ kg/m^3; C_{ice} is the ice-ocean drag coefficient, taken as 0.0055 (Meneghello et al., 2017); ρ_a is air density, taken as $\rho_a = 1.25$ kg/m^3; C_{air} is the air-ocean drag coefficient, taken as 0.00125 (Meneghello et al., 2017); $\mathbf{u_{air}}$ is the wind velocity; and $\mathbf{u_{rel}}$ is the relative velocity between the ice and the ocean, computed as $\mathbf{u_{rel}} = \mathbf{u_{ice}} - (\mathbf{u_{geo}} + \mathbf{u_{ek}})$ (Meneghello et al., 2017; Yang, 2006, 2009). The characterization of relative velocity follows analyses of the Beaufort Gyre where the ocean velocity is separated into an Ekman and a geostrophic component (Meneghello et al., 2017; Yang, 2006, 2009). For Bering Strait, there are additional components to the flow, such as tides and other barotropic flows, in addition to the balanced (geostrophic) and Ekman flows. Here we refer to $\mathbf{u_{geo}}$ as the "interior flow" to encompass all components of the ocean flow not associated with friction at the boundaries. Note that the DOT product includes ocean geostrophic velocity components at the same temporal and spatial resolutions (Armitage et al., 2016, 2017); however, due to the likely underestimation of these flows (inferred in Section 3.1), we do not use them in our calculations. To understand how this quantification of surface stress is sensitive to different interior flows, we examine three cases: 0 m/s, 0.1 m/s interior flow to the north, and interior flow equal to the bottom velocities (Figure 3d), the latter of which is a reasonable assumption given that flow through Bering Strait is approximately barotropic below 10–15 m depth (Roach et al., 1995).

3. Dynamics of Flow Through Bering Strait

The monthly across-strait slope calculated from the DOT field indicates a correlation with the monthly along-strait bottom velocity from 2003 to 2014 ($R = 0.53$, $p = 1.34\text{e}{-11}$; Figure 2). This suggests that the volume transport through the strait may be related in part to changes in the DOT field across the strait. We explore this further by analyzing the dynamics that govern transport with the steady state, depth-integrated, horizontal components of the momentum balance (e.g., Coachman & Aagaard, 1966):

$$-fV^r = -gH{\eta_x}^r + \frac{{\tau_{sfc}}^{x,r} - {\tau_{bot}}^{x,r}}{\rho}, \quad (2)$$

$$fU^r = -gH{\eta_y}^r + \frac{{\tau_{sfc}}^{y,r} - {\tau_{bot}}^{y,r}}{\rho}, \quad (3)$$

where f is the Coriolis parameter ($f = 1.46 \times 10^{-4}$ s^{-1} at the latitude of Bering Strait); $U^r = \int_{-H}^{0} u^r\, dz$; $V^r = \int_{-H}^{0} v^r\, dz$, and u^r and v^r are the across- and along-strait components of the ocean velocity, respectively; g is

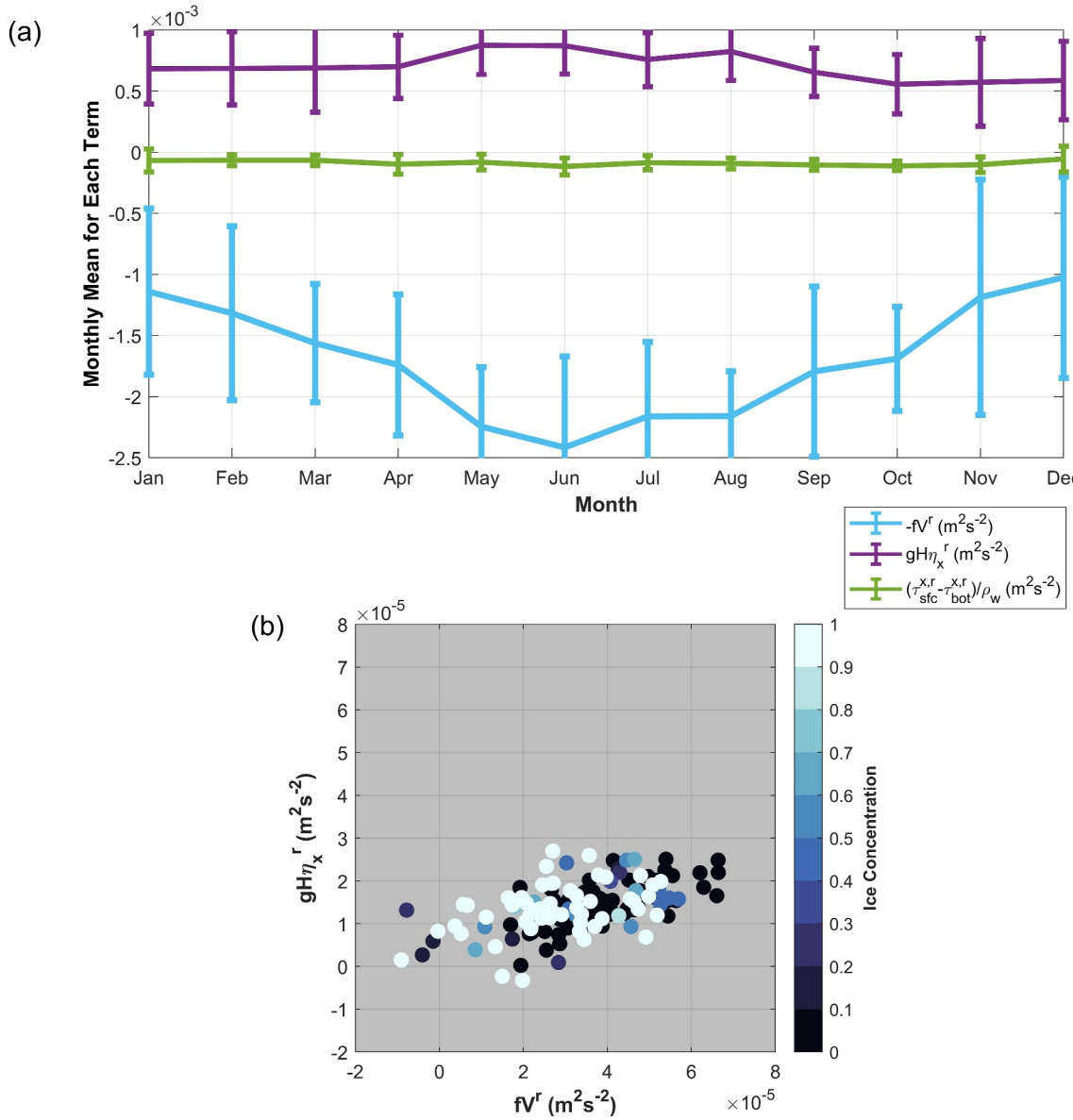

Figure 4. (a) Monthly climatology over 2003–2014 for the Coriolis term (cyan), pressure gradient term (purple), and stresses term with the surface stress calculated assuming a northward interior flow of 0.1 m/s (green) in the across-strait balance, Equation 2. The error bars are one standard deviation. (b) Monthly comparison of the Coriolis term (fV^r) versus the pressure gradient term $\left(gH\eta_x{}^r\right)$ where each dot is 1 month between 2003 and 2014 and shaded according to the average ice concentration in Bering Strait during that month.

gravitational acceleration; H is depth (approximately 50 m in Bering Strait). Lastly, $\boldsymbol{\tau_{sfc}}^{\mathbf{r}}$ is the rotated surface stress; $\boldsymbol{\tau_{bot}}^{\mathbf{r}}$ is the rotated bottom stress, given by $\tau^r_{\mathbf{bot}} = \rho C_{bot} |\mathbf{u}^{\mathbf{r}}_{\mathbf{bot}}| (\mathbf{u}^{\mathbf{r}}_{\mathbf{bot}})$ where C_{bot} is the ocean-bottom drag coefficient, taken as 0.0023 (Couto et al., 2020), and $\mathbf{u}^{\mathbf{r}}_{\mathbf{bot}}$ is the rotated bottom ocean velocity. In the next section, we will simplify Equation 2 and analyze how the simplified balance holds given observations local to Bering Strait.

3.1. Geostrophic Balance in the Across-Strait Direction

The across-strait balance is predominantly geostrophic, that is, the dominant balance is between the first two terms of Equation 2 (Figure 4a). Using the DOT data and the mooring data, we assess the geostrophic balance in the across-strait direction by quantifying how the across-strait slope compares to observed monthly bottom velocities (rotated, such that they are in the along-strait direction) through the strait. Over 2003–2014, there is a

moderate correlation ($R = 0.53$, $p = 1.3e{-}11$) between the across-strait slope and along-strait bottom velocities (Figure 4b). This moderate correlation in part reflects the similar seasonal cycles of the across-strait slope to that of the bottom velocities (Figure 2b) where the across-strait slope is maximized in summer when bottom velocities are faster and the across-strait slope is lower in winter when the bottom velocities are slower. While ocean transport and $\eta_x{}^r$ have strong seasonalities, the relation between the across-strait slope and the along-strait velocities does not vary based on sea ice cover, suggesting that the geostrophically balanced component of flow in the strait does not vary seasonally.

The correlation between the across-strait slope and the bottom velocity at Bering Strait suggests that some component of flow is in geostrophic balance. However, an estimate of the geostrophic flow using the across-strait slope (i.e., the second term of Equation 2) is only about 40% of the magnitude of the observed depth-integrated along-strait flow (Figure 4b). This might be due to the coarse resolution of the DOT product in the vicinity of Bering Strait. There are three grid boxes across the strait, meaning there are likely unresolved variations in the DOT field across Bering Strait. Another reason for the underestimation is that there are additional components to the bottom velocity through Bering Strait beyond the geostrophic component, such as those associated with time-varying, barotropic flow, strait geometry, and friction, that we are unable to characterize and remove before assessing the dynamical balance.

The along-strait balance (Equation 3) has also been used to explore the dynamics of flow through Bering Strait (e.g., Couto et al., 2020; Woodgate, 2018). We completed a similar analysis for the along-strait balance, examining both the geostrophic balance and a balance between the Coriolis term and the stress term. We did not find a strong relation in either case. Therefore, we focus on the across-strait slope and processes that may influence transport through modifying η_x^r. There are several mechanisms that could influence the magnitude of η_x^r such as local surface stress, buoyancy gradients, and large scale pressure differences between the Pacific and Arctic Oceans. For the remainder of this paper, we will focus on understanding the influence of local sea ice conditions on η_x^r and transport through Bering Strait via the local surface stress.

3.2. Ekman Transport in the Across-Strait Direction

We concluded in the previous section that some component of flow through Bering Strait is balanced by the across-strait slope, and it is well known that a locally applied along-strait surface stress can generate an across-strait slope via Ekman transport. Our goal is to explore how the local along-strait surface stress relates to the across-strait slope, and how this relation might vary based on local sea ice conditions. In the absence of sea ice, the wind stress corresponds to the across-strait slope (Figure 5a) where the across-strait slope increases as the along-strait winds increase to the north.

We find a statistically significant northward trend in local winds (99% confidence) over 2003–2021 (Figure 3b). Following the scaling introduced by Woodgate (2018, their Section 5.2), we estimate that a northward wind trend of 0.45 ± 0.12 m/s/decade (Figure 3b) would correspond to a bottom velocity trend of $2.8 \times 10^{-4} \pm 2.1 \times 10^{-5}$ m/s/decade, which is two orders of magnitude smaller than the observed trend in bottom velocity. This suggests that the observed increase in local winds to the north does not account for the observed northward increase in bottom velocity. Note also that local winds are generally to the south while transport is to the north (Figure 3), so the wind effect is to modulate the northward ocean flow.

When estimating the trend in bottom velocity associated with increased northward winds, we characterized the surface stress as wind stress on open ocean. However, this is not the case in Bering Strait year-round as sea ice is present from roughly November to June. When sea ice is present, the surface stress can strongly depend on the strength of the interior flow, which can be of the same order of magnitude as the ice motion (Figures 5b, 5c, and 5d); in the absence of sea ice, the ocean flow can be neglected relative to the much faster wind speeds in the calculation of surface stress. For sea ice concentrations close to one, in the case of no interior flow, surface stresses are generally northward (Figure 5b and dotted black line in Figure 5d). Since the winds over Bering Strait are generally to the south, even while sea ice motion is to the north, the northward ocean flow must be playing a role in driving sea ice to the north and any calculation of surface stress must assume non-zero ocean flow. As the interior ocean flow increases to the north (Figures 5c and 5d, and Figure S2 in Supporting Information S1) under high sea ice concentrations, the surface stress becomes increasingly southward, leading to a decrease in the balanced component of northward transport via increased Ekman transport to the west. The sensitivity of surface

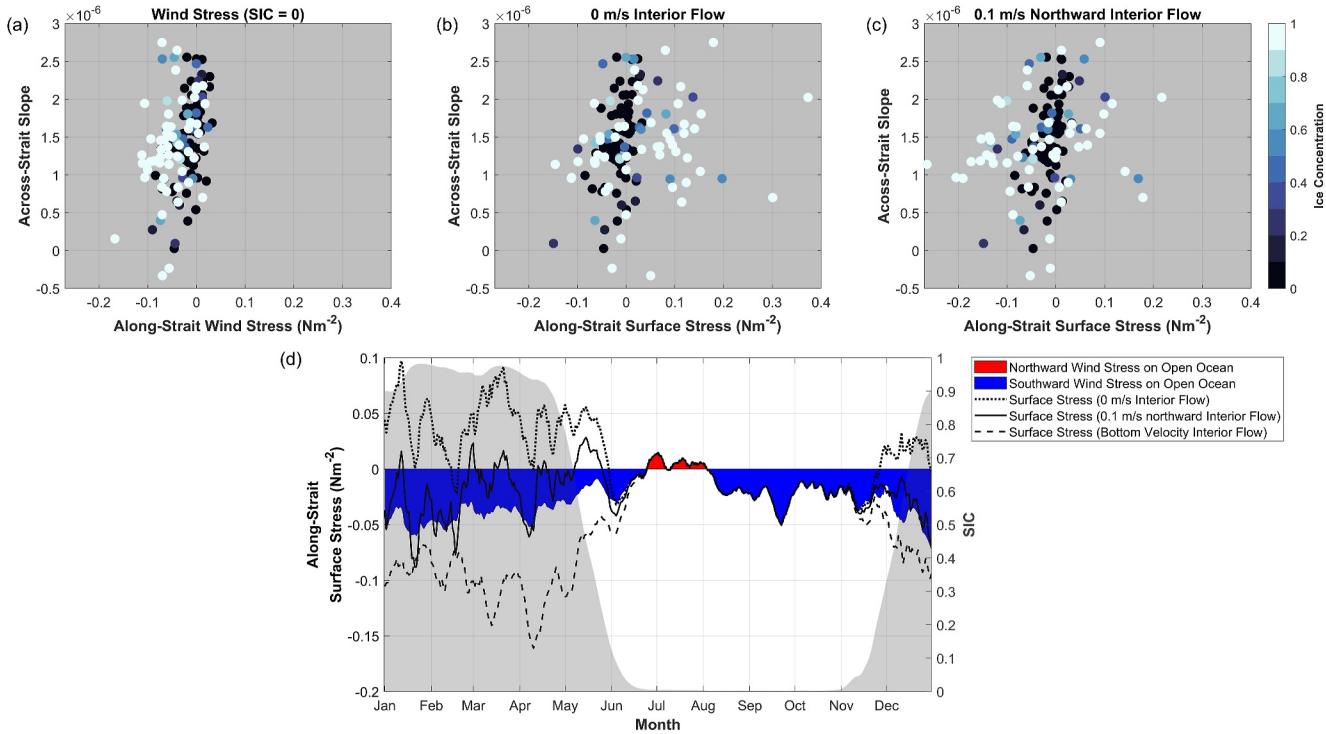

Figure 5. Monthly across-strait dynamic ocean topography slope from 2003–2014 versus the monthly mean of panel (a) along-strait wind stress ignoring the presence of sea ice (i.e., SIC = 0 in Equation 1), (b) along-strait surface stress calculated assuming zero interior flow and (c) along-strait surface stress calculated assuming an interior flow of 0.1 m/s to the north. Shading represents the monthly mean sea ice concentration. (d) 10-day running average of the daily climatology from 2003–2021 of along-strait wind stress on open ocean (southward in blue and northward in red), along-strait surface stress computed with zero interior flow (dotted black), 0.1 m/s to the north (solid black), and the bottom velocity (dashed black). The 10-day running average of the daily climatology for sea ice concentration is shaded in gray.

stress to the presence of sea ice highlights that our understanding of surface dynamics in Bering Strait is incomplete without a more detailed understanding of the strength and variability of the interior flow.

Using the same scaling from Woodgate (2018, their Section 5.2) as before, we find a statistically significant northward trend in surface stress assuming an interior flow of 0.1 m/s (90% confidence) over 2003–2021 (Figure 3d). We estimate the northward trend in surface stress (assuming an interior flow of 0.1 m/s) of 0.008 ± 0.005 N/m^2/decade (Figure 3b) would correspond to a bottom velocity trend of $7.1 \times 10^{-3} \pm 4.5 \times 10^{-3}$ N/m^2/decade, which is approximately 35% of the observed trend in bottom velocity. For surface stress calculated assuming the interior flow is equal to the bottom velocity, the surface stress trend accounts for $\sim$ 27% of the observed increase in bottom velocity. This suggests that changes in sea ice may contribute to the observed changes in bottom velocity, which we explore further in the next section.

4. Influence of Sea Ice on Transport via Surface Stress

Long-term northward trends in surface stress suggest that changes in surface stress may be contributing, in part, to the observed increase in northward transport through Bering Strait. We explore how the sensitivity of surface-ocean stress to sea-ice conditions might translate to influencing transport through Bering Strait in context with the loss of regional sea ice over recent decades. To do this, we first analyze the variability in along-strait winds, sea ice motion, bottom velocity, and across-strait Ekman transport, $M_{ek}^{x,r} = \tau_{sfc}^{y,r}/f$, over the course of a seasonal cycle. We focus on 2006 as a representative year to show how the relation between variables differs under ice cover versus open water on daily to weekly timescales.

When sea ice is absent, we find that northward increases in wind lead to increases in northward flow through the strait via the inferred increased Ekman transport to the east (Figure 6). This is consistent with the previous discussion of winds influencing variability in northward transport during days of open water. When sea ice is present in Bering Strait, we find that large increases in wind (to the north or south) are associated with increases in

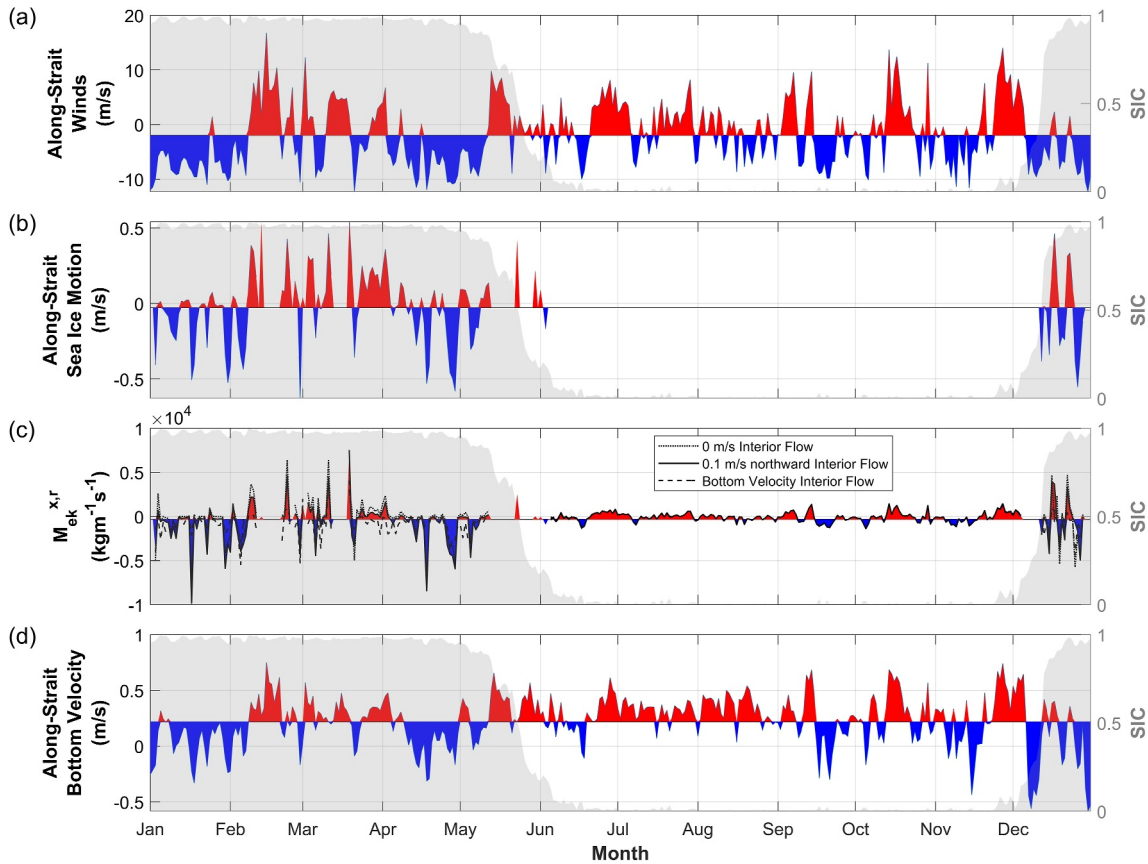

Figure 6. Daily anomalies during 2006 of (a) along-strait winds, (b) along-strait sea ice motion, (c) across-strait Ekman transport, $M_{ek}^{x,r}$, assuming no interior flow (dotted line), a northward interior flow of 0.1 m/s (solid line, red/blue shading), and interior flow equal to the bottom velocity (dashed line), and (d) along-strait bottom velocity all local to Bering Strait. Gray shading is daily sea ice concentration. Anomalies shaded with red indicate northward anomalies in panels (a, b, and d), and eastward anomalies in panel (c) Anomalies shaded with blue denote southward and westward anomalies in the respective panels.

sea ice motion, inferred Ekman transport, and bottom velocity in the respective directions. Additionally, the magnitude of the inferred Ekman transport in the presence of sea ice varies according to the assumed interior flow. When we assume no interior flow, the inferred Ekman transport under sea ice is stronger to the east than the cases of 0.1 m/s ocean flow to the north or taking ocean flow into account using the measured bottom velocity. Additionally, all cases illustrate variability that is consistent with a relationship to volume transport (i.e., inferred eastward Ekman transport and northward bottom velocities occur simultaneously). The greater inferred westward Ekman transport under sea ice than open water conditions in all cases could be one reason we observe weaker transport in the winter. We also find that all cases of interior flow show larger variability in inferred Ekman transport between sea ice-free and sea ice-covered conditions. However, we observe comparable variations in bottom velocity between when sea ice is present versus absent (Figure 6). This could indicate that remote effects of local wind-forcing changes have a dominant influence on the flow. Given that surface stress is sensitive to the presence of sea ice, it follows that the loss of sea ice might lead to changes in transport through increased interaction with the winds via increased open water days.

The number of open water days in the Bering Strait region have been increasing over the last several decades (Serreze et al., 2016). We explore the possibility of whether the increase in the number of open water days has an effect on the transport through associated changes in surface stress imparted to the ocean. We use a SIC threshold of 15% over the region specified in Section 2.3 to define the day of sea ice retreat and advance locally each year (Cavalieri et al., 1991), where days of open water are those between sea ice retreat and sea ice advance. However, we find no trend in the annual mean along-strait surface stress assuming an interior flow of 0.1 m/s over ice-covered days (Figure 7a) or over open water days (Figure 7b). We do find a decrease in the cumulative southward surface stress at the strait during the ice-covered period, due to the trend of fewer days with ice cover each

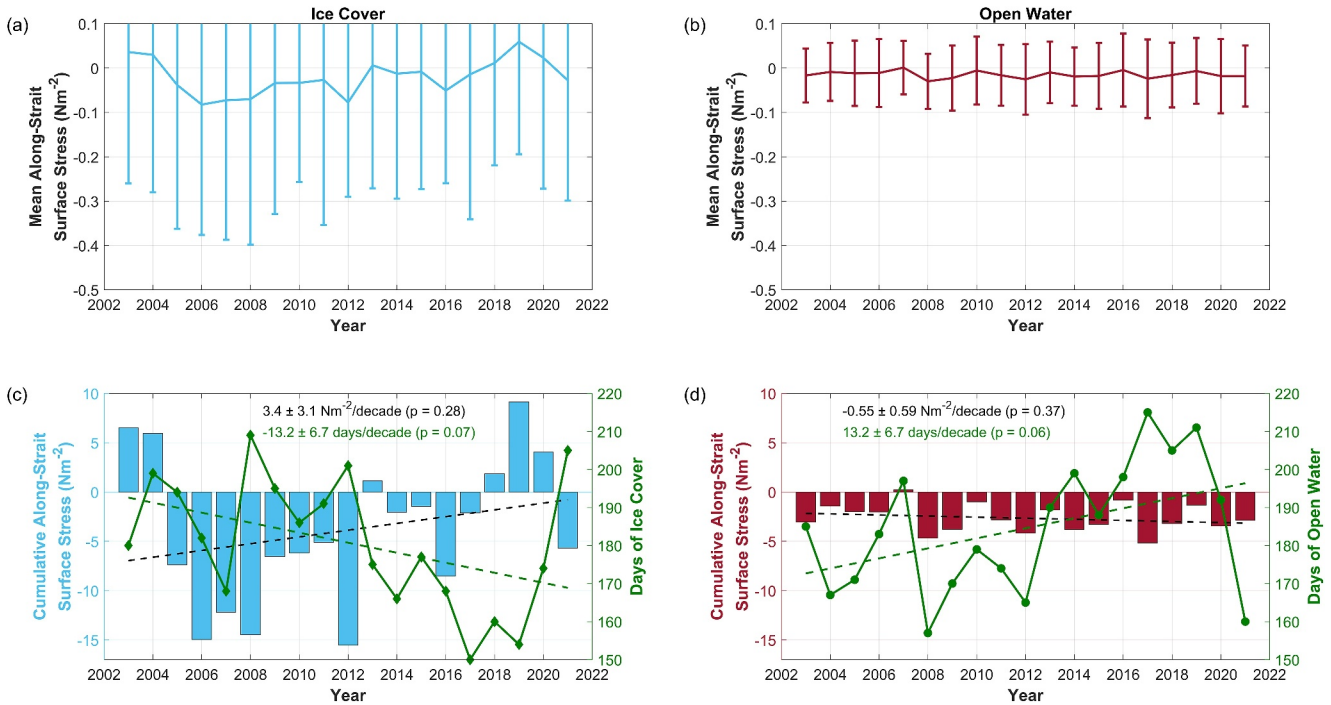

Figure 7. (a) Mean along-strait surface stress assuming an interior flow of 0.1 m/s for ice-covered days. (b) Mean along-strait surface stress assuming an interior flow of 0.1 m/s for open water days. Error bars show one standard deviation. (c) Cumulative along-strait surface stress assuming an interior flow of 0.1 m/s of daily averages for ice-covered days (blue) and the number of days of ice cover each year (green) local to Bering Strait. The green dashed line shows the trend in days of ice cover ($p = 0.07$). The black dashed line shows the trend in cumulative along-strait surface stress for days of ice cover ($p = 0.28$). (d) Cumulative along-strait surface stress assuming an interior flow of 0.1 m/s of daily averages for open water days (red) and the number of days of open water each year (green) local to Bering Strait. The green dashed line shows the trend in open water days ($p = 0.06$). The black dashed line shows the trend in cumulative along-strait surface stress for days of open water ($p = 0.37$).

year (Figure 7c). This is compensated by an increase in the southward surface stress at the strait during the ice-free period as a result of the increasing trend in open water days per year (Figure 7d). In other words, the observed increase in Bering Strait throughflow is not associated with a reduction in southward surface stress due to the increasing number of open water days at the strait. A similar result is found for the case of assuming the interior flow is the bottom velocity, though the trends have higher p-values (Figure S3 in Supporting Information S1).

5. Summary and Discussion

Bering Strait is the only source of Pacific inflow for the Arctic Ocean, and the volume of Pacific water entering the Arctic has been increasing at 0.01 Sv/yr over the last few decades (Woodgate, 2018). We find that some component of flow through Bering Strait is balanced with the across-strait DOT gradient year-round. This is consistent with the findings of Cherniawsky et al. (2005) who examined only ice-free periods. In the framework of geostrophic balance, the across-strait slope balances some component of the along-strait velocity through Bering Strait, and several processes can contribute to an across-strait slope.

We focus on how local winds and sea ice conditions contribute to the along-strait surface stress and generate an across-strait slope via inferred Ekman transport. We find that as the along-strait winds increase to the north, the across-strait slope steepens due to increased Ekman transport to the east, and northward transport through the strait increases. Of importance is that local winds in Bering Strait are generally to the south such that increases in volume transport correspond to a weakening of winds to the south as opposed to strengthening of winds to the north. One added complexity in this system is that Bering Strait is ice covered from around November to June, when ocean surface stress is modulated by the presence of sea ice. We find that quantifying the surface stress local to Bering Strait under ice cover is challenging given that the surface stress characterization is sensitive to the interior ocean flow. When we assume no interior flow, the sea ice motion and surface stress are northward, while the winds are predominantly to the south. This implies that the northward ocean flow, at least in part, drives the

sea ice and, therefore, should be considered when calculating surface stress. For interior flows increasing to the north, the surface stress increases to the south (i.e., westward Ekman transport increases) and northward ocean transport decreases. Similar to how sea ice in the Beaufort Gyre contributes to gyre spin down through divergent Ekman transport, sea ice in Bering Strait weakens northward flow through enhanced westward Ekman transport. In both systems, the presence of sea ice contributes to the reduced strength of each during the winter. Furthermore, this suggests that the strong correlation between local winds and the observed bottom velocities in Bering Strait might be misleading in the presence of sea ice as both the ocean flow and local winds influence the sea ice motion and surface stress. It is possible that the signal in local winds correlating to bottom velocity is indicative of the relationship between changes in the large-scale atmospheric circulation and the pressure head component driving flow through Bering Strait (Danielson et al., 2014; Nguyen et al., 2020; Zhang et al., 2020).

The sensitivity of surface stress to the presence of sea ice suggests that with the increasing number of open water days in Bering Strait, there may be changes in surface stress that would influence transport. However, we do not find a trend in the annual mean surface stress. It would appear that changes in the duration of ice cover local to Bering Strait are not leading to changes in the stress input that affect transport through the strait via changes in Ekman transport. It is possible that these processes are contributing to changes in remote regions associated with the pressure head, thereby affecting the across-strait slope and the volume transport through Bering Strait.

Data Availability Statement

Arctic dynamic topography data were provided by the Centre for Polar Observation and Modelling, University College London (www.cpom.ucl.ac.uk/dynamic_topography) (Armitage et al., 2016, 2017). Data from the A3 and A4 moorings in Bering Strait are available at the National Centers for Environmental Information (https://www.ncei.noaa.gov/) and also on the Bering Strait project website: https://psc.apl.washington.edu/BeringStrait.html (Woodgate, 2018; Woodgate et al., 2015; Woodgate & Peralta-Ferriz, 2021). ECMWF ERA5 winds are available through the Copernicus Climate Change Service (Hersbach et al., 2023). Sea ice concentration data are from the National Snow and Ice Data Center (NSIDC) (Meier et al., 2021). Bathymetry data are available through the General Bathymetric Chart of the Oceans (GEBCO Compilation Group, 2022, 2022).

Acknowledgments
Funding for this study was provided by the National Science Foundation, Division of Polar Programs under Grant 2053003. We thank Rebecca Woodgate (University of Washington) and collaborators for maintaining the long-term mooring record in Bering Strait and making the data available.

References

Aagaard, K., & Carmack, E. C. (1989). The role of sea ice and other fresh water in the Arctic circulation. *Journal of Geophysical Research*, *94*(C10), 14485–14498. https://doi.org/10.1029/JC094iC10p14485

Aagaard, K., Coachman, L., & Carmack, E. (1981). On the halocline of the Arctic Ocean. *Deep-Sea Research, Part A: Oceanographic Research Papers*, *28*(6), 529–545. https://doi.org/10.1016/0198-0149(81)90115-1

Aagaard, K., Weingartner, T. J., Danielson, S. L., Woodgate, R. A., Johnson, G. C., & Whitledge, T. E. (2006). Some controls on flow and salinity in Bering Strait. *Geophysical Research Letters*, *33*(19), L19602. https://doi.org/10.1029/2006GL026612

Armitage, T. W., Bacon, S., Ridout, A. L., Petty, A. A., Wolbach, S., & Tsamados, M. (2017). Arctic Ocean surface geostrophic circulation 2003–2014. *The Cryosphere*, *11*(4), 1767–1780. https://doi.org/10.5194/tc-11-1767-2017

Armitage, T. W., Bacon, S., Ridout, A. L., Thomas, S. F., Aksenov, Y., & Wingham, D. J. (2016). Arctic sea surface height variability and change from satellite radar altimetry and GRACE, 2003–2014. *Journal of Geophysical Research: Oceans*, *121*(6), 4303–4322. https://doi.org/10.1002/2015JC011579

Cavalieri, D. J., Crawford, J. P., Drinkwater, M. R., Eppler, D. T., Farmer, L. D., Jentz, R. R., & Wackerman, C. C. (1991). Aircraft active and passive microwave validation of sea ice concentration from the Defense Meteorological Satellite Program special sensor microwave imager. *Journal of Geophysical Research: Oceans*, *96*(C12), 21989–22008. https://doi.org/10.1029/91jc02335

Cessi, P. (2020). Control of Bering Strait transport by the meridional overturning circulation. *Journal of Physical Oceanography*, *50*(7), 1853–1870. https://doi.org/10.1175/JPO-D-20-0026.1

Cherniawsky, J., Crawford, W., Nikitin, O., & Carmack, E. (2005). Bering Strait transports from satellite altimetry. *Journal of Marine Research*, *63*(5), 887–900. https://doi.org/10.1357/002224005774464201

Coachman, L. K., & Aagaard, K. (1966). On the water exchange through Bering Strait. *Limnology & Oceanography*, *11*(1), 44–59. https://doi.org/10.4319/lo.1966.11.1.0044

Couto, N., Alford, M. H., MacKinnon, J., & Mickett, J. B. (2020). Mixing rates and bottom drag in Bering Strait. *Journal of Physical Oceanography*, *50*(3), 809–825. https://doi.org/10.1175/JPO-D-19-0154.1

Danielson, S. L., Weingartner, T. J., Hedstrom, K. S., Aagaard, K., Woodgate, R., Curchitser, E., & Stabeno, P. J. (2014). Coupled wind-forced controls of the Bering–Chukchi shelf circulation and the Bering Strait throughflow: Ekman transport, continental shelf waves, and variations of the Pacific–Arctic sea surface height gradient. *Progress in Oceanography*, *125*, 40–61. https://doi.org/10.1016/j.pocean.2014.04.006

Dewey, S., Morison, J., Kwok, R., Dickinson, S., Morison, D., & Andersen, R. (2018). Arctic ice-ocean coupling and gyre equilibration observed with remote sensing. *Geophysical Research Letters*, *45*(3), 1499–1508. https://doi.org/10.1002/2017GL076229

Doglioni, F., Ricker, R., Rabe, B., Barth, A., Troupin, C., & Kanzow, T. (2023). Sea surface height anomaly and geostrophic current velocity from altimetry measurements over the Arctic Ocean (2011–2020). *Earth System Science Data*, *15*(1), 225–263. https://doi.org/10.5194/essd-15-225-2023

GEBCO Compilation Group 2022. (2022). The GEBCO_2022 Grid - A continuous terrain model of the global oceans and land. (Version 1) [Dataset]. *NERC EDS British Oceanographic Data Centre NOC*. https://doi.org/10.5285/E0F0BB80-AB44-2739-E053-6C86ABC0289C

Hersbach, H., Bell, B., Berrisford, P., Biavati, G., Horányi, A., Sabater, J. M., et al. (2023). ERA5 hourly data on single levels from 1940 to present [Dataset]. *Copernicus Climate Change Service (C3S) Climate Data Store (CDS)*. https://doi.org/10.24381/cds.adbb2d47

Lin, P., Pickart, R. S., Heorton, H., Tsamados, M., Itoh, M., & Kikuchi, T. (2023). Recent state transition of the Arctic Ocean's Beaufort Gyre. *Nature Geoscience*, *16*(6), 1–7. https://doi.org/10.1038/s41561-023-01184-5

Lu, K., Danielson, S., Hedstrom, K., & Weingartner, T. (2020). Assessing the role of oceanic heat fluxes on ice ablation of the central Chukchi Sea Shelf. *Progress in Oceanography*, *184*, 102313. https://doi.org/10.1016/j.pocean.2020.102313

Meier, W. N., Fetterer, F., Windnagel, A. K., & Stewart, J. S. (2021). NOAA/NSIDC Climate Data Record of Passive Microwave Sea Ice Concentration, Version 4 [Dataset]. *National Snow and Ice Data Center*. https://nsidc.org/data/G02202/versions/4

Meneghello, G., Marshall, J., Cole, S. T., & Timmermans, M.-L. (2017). Observational inferences of lateral eddy diffusivity in the halocline of the Beaufort Gyre. *Geophysical Research Letters*, *44*(24), 12–331. https://doi.org/10.1002/2017GL075126

Meneghello, G., Marshall, J., Timmermans, M.-L., & Scott, J. (2018). Observations of seasonal upwelling and downwelling in the Beaufort Sea mediated by sea ice. *Journal of Physical Oceanography*, *48*(4), 795–805. https://doi.org/10.1175/JPO-D-17-0188.1

Nguyen, A. T., Woodgate, R. A., & Heimbach, P. (2020). Elucidating large-scale atmospheric controls on Bering Strait throughflow variability using a data-constrained ocean model and its adjoint. *Journal of Geophysical Research: Oceans*, *125*(9), e2020JC016213. https://doi.org/10.1029/2020JC016213

Pawlowicz, R., Beardsley, B., & Lentz, S. (2002). Classical tidal harmonic analysis including error estimates in MATLAB using T_TIDE. *Computers & Geosciences*, *28*(8), 929–937. https://doi.org/10.1016/S0098-3004(02)00013-4

Peralta-Ferriz, C., & Woodgate, R. A. (2017). The dominant role of the East Siberian Sea in driving the oceanic flow through the Bering Strait—Conclusions from GRACE ocean mass satellite data and in situ mooring observations between 2002 and 2016. *Geophysical Research Letters*, *44*(22), 11–472. https://doi.org/10.1002/2017GL075179

Proshutinsky, A., Bourke, R., & McLaughlin, F. (2002). The role of the Beaufort Gyre in Arctic climate variability: Seasonal to decadal climate scales. *Geophysical Research Letters*, *29*(23), 2100. https://doi.org/10.1029/2002GL015847

Roach, A., Aagaard, K., Pease, C., Salo, S., Weingartner, T., Pavlov, V., & Kulakov, M. (1995). Direct measurements of transport and water properties through the Bering Strait. *Journal of Geophysical Research*, *100*(C9), 18443–18457. https://doi.org/10.1029/95JC01673

Serreze, M. C., Barrett, A. P., Slater, A. G., Woodgate, R. A., Aagaard, K., Lammers, R. B., et al. (2006). The large-scale freshwater cycle of the Arctic. *Journal of Geophysical Research*, *111*(C11), C11010. https://doi.org/10.1029/2005JC003424

Serreze, M. C., Crawford, A. D., Stroeve, J. C., Barrett, A. P., & Woodgate, R. A. (2016). Variability, trends, and predictability of seasonal sea ice retreat and advance in the Chukchi Sea. *Journal of Geophysical Research: Oceans*, *121*(10), 7308–7325. https://doi.org/10.1002/2016JC011977

Shaw, W., Stanton, T., McPhee, M., Morison, J., & Martinson, D. (2009). Role of the upper ocean in the energy budget of Arctic sea ice during SHEBA. *Journal of Geophysical Research*, *114*(C6), C06012. https://doi.org/10.1029/2008JC004991

Shimada, K., Kamoshida, T., Itoh, M., Nishino, S., Carmack, E., McLaughlin, F., et al. (2006). Pacific Ocean inflow: Influence on catastrophic reduction of sea ice cover in the Arctic Ocean. *Geophysical Research Letters*, *33*(8), L08605. https://doi.org/10.1029/2005GL025624

Woodgate, R. A. (2018). Increases in the Pacific inflow to the Arctic from 1990 to 2015, and insights into seasonal trends and driving mechanisms from year-round Bering Strait mooring data. *Progress in Oceanography*, *160*, 124–154. https://doi.org/10.1016/j.pocean.2017.12.007

Woodgate, R. A., & Peralta-Ferriz, C. (2021). Warming and freshening of the Pacific inflow to the Arctic from 1990-2019 implying dramatic shoaling in Pacific winter water ventilation of the Arctic water column. *Geophysical Research Letters*, *48*(9), e2021GL092528. https://doi.org/10.1029/2021GL092528

Woodgate, R. A., Stafford, K. M., & Prahl, F. G. (2015). A synthesis of year-round interdisciplinary mooring measurements in the Bering Strait (1990–2014) and the RUSALCA years (2004–2011). *Oceanography*, *28*(3), 46–67. https://doi.org/10.5670/oceanog.2015.57

Woodgate, R. A., Weingartner, T., & Lindsay, R. (2010). The 2007 Bering Strait oceanic heat flux and anomalous Arctic sea-ice retreat. *Geophysical Research Letters*, *37*(1), L01602. https://doi.org/10.1029/2009GL041621

Yang, J. (2006). The seasonal variability of the Arctic Ocean Ekman transport and its role in the mixed layer heat and salt fluxes. *Journal of Climate*, *19*(20), 5366–5387. https://doi.org/10.1175/JCLI3892.1

Yang, J. (2009). Seasonal and interannual variability of downwelling in the Beaufort Sea. *Journal of Geophysical Research*, *114*(C1), C00A14. https://doi.org/10.1029/2008JC005084

Zhang, W., Wang, Q., Wang, X., & Danilov, S. (2020). Mechanisms driving the interannual variability of the Bering Strait throughflow. *Journal of Geophysical Research: Oceans*, *125*(2), e2019JC015308. https://doi.org/10.1029/2019JC015308